International Journal of Heat and Mass Transfer

Temperatures near the interface between an ideal heat exchanger and a thermal buffer tube or pulse tube

Konstantin I. Matveev, Gregory W. Swift*, Scott Backhaus

Condensed Matter and Thermal Physics Group, Los Alamos National Laboratory,

MS K764, Los Alamos, NM 87545, USA

Abstract

A thermal buffer tube (or pulse tube) thermally isolates two heat exchangers at different temperatures in a thermoacoustic engine or refrigerator while allowing the flow of acoustic power. For many heat transport mechanisms, the quality of the thermal isolation depends on the time-averaged mean temperature distribution in the thermal buffer tube, which is determined by boundary conditions set up by the heat exchangers. However, finite-amplitude effects within one peak-to-peak gas displacement of the heat exchangers can lead to significant modification of the thermal boundary conditions and thus the heat transport. To explore these effects, measured mean temperature profiles in the vicinity of the interface between a heat exchanger and thermal buffer tube are reported for a broad range of acoustic and thermal conditions. A one-dimensional Lagrangian model is developed to predict the mean temperature distribution, and reasonable agreement between experimental data and model results is found for the majority of the acoustic conditions considered.

Keywords: Thermoacoustics; Pulse tube; Thermal buffer tube; Joining conditions; Interface

* Corresponding author. Tel.: +1 505 665 0640; fax: +1 505 665 7652.
E-mail address: swift@lanl.gov (G.W. Swift).

Nomenclature

c_p	specific heat
h	width of computational gas parcels
$\dot{H}$	enthalpy flux
k	thermal conductivity
K	heat transfer coefficient of the heat exchanger
$\dot{m}$	mass flux
m_0	mass per unit area of computational gas parcels
p	pressure
R	specific gas constant
t	time
T	temperature
u	velocity
x	position coordinate
x_1	amplitude of gas motion

Greek symbols

δT	discontinuity in temperature
γ	ratio of specific heats
θ	phase by which pressure oscillation leads velocity oscillation
ω	angular frequency
ρ	density
τ	period

Subscripts

HX	heat exchanger

i, j	indices to label a computational gas parcel
m	mean
1	amplitude of sinusoidal motion
N	index to the final computational gas parcel
p	piston
0	indicating the molecular thermal conductivity
ef	indicating the effective thermal conductivity

1. Introduction

Stirling and thermoacoustic engines and refrigerators (including pulse tube refrigerators) are energy conversion devices that either produce acoustic energy from a mean temperature gradient or use acoustic energy to pump thermal energy up such a gradient. Significant effort has been devoted to developing tools for predicting their performance. However, at the present time, only the low-amplitude (linear) regime is well understood and accurately predicted, while finite-amplitude effects reduce the accuracy of the predictions at higher power density [1].

One such finite-amplitude effect modifies the mean temperature distribution at the interface between a heat exchanger and a thermal buffer tube (TBT) or pulse tube, which are essentially open tubes located between two heat exchangers at different temperatures in some of these thermoacoustic engines and refrigerators [2]. The role of the TBT is to pass acoustic energy flow while minimizing heat transport due to boundary layer "entropy flow," heat conduction through the gas and the tube walls, radiation, and mass streaming caused by nonlinear acoustics [1]. As a gas parcel moves from the isothermal environment inside an ideal heat exchanger to the nearly isentropic space inside a TBT, it leaves the heat exchanger with the heat exchanger's temperature. However, depending on the acoustic conditions imposed on the system, it may return with a different temperature, resulting in an irreversible thermodynamic loss of acoustic energy due to heat transfer across a non-negligible temperature difference. Models for the interface loss have been introduced [3-6] and are widely accepted and incorporated in design software, although verification with experiments on interfaces in isolation is lacking.

The distortion of the mean temperature distribution near the ends of the TBT lies at the heart of the interface-loss models and also contributes to unwanted thermal loss by steepening the temperature gradient in the center of TBTs. This distortion was observed in experiments by Storch et al. [7] and Swift [8]. In the former experiment, the central temperature gradient in the pulse tube was doubled by this phenomenon. De Boer [9] analyzed temperature profiles in a pulse tube using an idealized four-step thermodynamic cycle. Kittel [10] proposed a simple expression for the maximum mean temperature overshoot between the gas and the nearby heat exchanger for one particular acoustic condition. Using simple arguments, Swift [1] gave an expression for the mean temperature discontinuity between the gas and the heat exchanger as a

function of the acoustic variables, the ratio of specific heat capacities of the working gas, the heat exchanger temperature, and the temperature gradient in the gas deep inside the TBT.

Some insight into this phenomenon can be gained from the idealized temperature–position trajectories of gas parcels in the vicinity of the heat exchanger, as shown in Fig. 1. The isothermal heat exchanger has a fixed temperature T_{HX}. The space in the TBT is thermally stratified, and a constant mean temperature gradient exists in the gas beyond a peak-to-peak displacement away from the heat exchanger. One-dimensional acoustic motion is assumed, and heat conduction between gas parcels and viscosity are neglected. However, when a gas parcel enters the heat exchanger, it instantaneously acquires the heat exchanger temperature. The acoustic wavelength is much larger than the peak-to-peak gas displacement, so changes in the acoustic velocity due to compressibility can be ignored. In Fig. 1b, acoustic pressure lags acoustic velocity by 90^o. Therefore, both pressure and temperature oscillations are in phase with the gas-parcel displacement. The "particular" parcel of gas, indicated by the slanting bold line in Fig. 1b, just touches the heat exchanger at its leftmost position and acquires an instantaneous temperature of T_{HX} at that time moment. Parcels to the right have similar trajectories, while parcels to the left follow a portion of the "particular" parcel's trajectory when outside the heat exchanger and have temperature T_{HX} when inside. Thus, a curved mean temperature distribution appears within a peak-to-peak displacement of the heat exchanger. If the mean temperature distribution to the right of this zone is extrapolated to the heat exchanger interface, there is a temperature discontinuity δT_m between the mean gas temperature and the heat exchanger temperature T_{HX}, caused by the acoustic oscillations. The temperature gradient in the axial center of the TBT is altered by δT_m at both ends.

Figure 1c depicts the same process when the acoustic pressure and velocity are in phase. Pressure and temperature oscillations lead the gas parcel displacement by 90^o, and the result is an elliptical trajectory for the "particular" gas parcel, with an instantaneous temperature of T_{HX} at its leftmost position as shown by the bold ellipse in Figure 1c. Again, parcels to the right of the particular parcel follow similar trajectories while parcels to the left follow truncated ellipses with a temperature of T_{HX} while inside of the heat exchanger. The mean temperature profile inside the peak-to-peak zone again acquires a curved shape, which is different from that in Fig. 1b.

The temperature discontinuity at the heat exchanger interface obtained by Swift [1] is

$$\delta T_m = -T_{HX}\,\frac{\gamma-1}{\gamma}\,\frac{p_1}{p_m}\sin\theta - x_1\,\frac{dT_m}{dx}\,, \tag{1}$$

where γ is the ratio of specific heats of the gas, p_1 is the amplitude of the pressure fluctuation, p_m is the mean pressure, θ is the phase by which the pressure oscillations lead the velocity oscillations (with positive velocity in the positive-x direction), x_1 is the peak displacement, and dT_m / dx is the mean temperature gradient in the TBT beyond one peak-to-peak displacement. The analysis in [1] did not consider thermal conduction in the gas, which may reduce the temperature discontinuity in Eq. (1) significantly.

The main goal of this study is to observe the mean temperature distribution in the gas near the ends of a TBT for a broad range of acoustic and thermal conditions; such measurements have not previously been reported. The experimental system built for this purpose is described in Section 2. A mathematical model that predicts the mean temperature profiles by tracking gas parcels in time and space is outlined in Section 3. The idea of tracking gas parcels was discussed before, e.g., in [1,10], but no complete predictions of the mean temperature profiles were made. The methodology of our experiments and simulations is discussed in Section 4. Experimental and theoretical results are presented in Section 5, confirming previous ideas about the temperature end effect and demonstrating the importance of acoustic parameters, thermal boundary conditions, and heat conduction.

2. Experimental System

An overview of the experimental apparatus is shown in Fig. 2a. The main section is a vertically oriented TBT made from a 2.49-cm-i.d. stainless-steel tube. Above the TBT, a pair of pressure-balanced bellows driven by a linear motor produces acoustic oscillations in the TBT. A power amplifier, driven by the reference signal of a lock-in amplifier, supplies the electrical power to the linear motor. The system is typically filled with 3.45-bar helium gas, although nitrogen and argon were also used.

In order to generate a broad range of acoustic pressures, velocities, and relative phases, an adjustable acoustic network is attached to the lower end of the TBT. A 1.09-cm-i.d. tube of about one meter length attached to the bottom of the TBT through a valve forms a series combination of an acoustic inertance and resistance that connects to a 2.3-liter tank. A second valve and a shorter section of tubing provide a

resistive shunt around the longer inertance path. Details of such an acoustic network can be found in [11]. Such an acoustic network is analogous to an electrical impedance made of an inductor and variable resistor in series, these together being in parallel with a second variable resistor, this assembly being in series with a capacitor to ground. By adjusting the valve settings independently, the network impedance can be easily changed to generate different complex acoustic impedances in the experimental part of the system. With the variables used to describe the data later in this paper, this control of the complex acoustic impedance is equivalent to independent control of p_1/x_1 and of θ. Simultaneously, the amplitude of the oscillations is controlled by the power to the linear motor.

The acoustic wave in the system is monitored by piezoresistive pressure transducers at three locations: the lower end of the driving unit, the lower end of the TBT, and in the compliance. All transducers are flush mounted with the internal surfaces of the system components. The acoustic pressure signals are read with the same lock-in amplifier used to drive the linear motor. The acoustic pressure measurements in the tank and at the lower end of the TBT, along with a numerical model of the experimental system [12], allow the acoustic velocity and pressure to be determined throughout the TBT. The transducers are calibrated in the pressure range of interest using static pressure and a Bourdon-tube pressure gauge.

The heat exchangers are 5-cm-long copper cylinders with nineteen 3.18-mm-diameter circular channels drilled through, parallel to the direction of acoustic motion. Their temperature is set using either electrically powered band heaters or aluminum blocks ported for circulating water clamped to the outside of the heat exchangers. Only two out of three heat exchangers shown in Fig. 2a are used in this experiment; the heat exchanger between the driving unit and the guard tube is used in other experiments. The length of the TBT between the two experimental heat exchangers is about 30 cm, which is several times larger than the peak-to-peak displacement in the oscillating gas. Therefore, the temperature effects at the two ends of the tube do not interfere with each other. In order to minimize any radial heat leak that may affect the temperature distribution, 3 cm of ceramic-fiber insulation surrounds the outside of the TBT. At acoustic displacements comparable to or longer than the diameter of the channels drilled in the heat exchangers, strong jets are produced that would disrupt the thermal stratification in the TBT. Therefore, 2-mm-long flow straighteners comprising a few layers of copper mesh are employed at both ends of every heat exchanger.

A close-up of the experimental section used to determine the mean-temperature distribution in the gas near the heat exchanger is shown in Fig. 2b. A stack of several layers of copper screen having an overall thickness of 7.8 mm, a volumetric porosity of 0.79, and a hydraulic radius of 290 μm is placed at the very end of the TBT. (A few additional layers fill the short space between the screen stack and the flow straightener atop the nearby heat exchanger.) The screen stack is designed to fulfill two purposes. First, its heat capacity is high enough that it undergoes minimal temperature oscillations when gas parcels pass through and intensively exchange heat with the screen. Second, the hydraulic radius is small enough to force rapid thermal relaxation of the gas as it enters the screen so that the gas acquires the screen temperature in a length much less than the overall screen thickness. These two factors provide confidence that gas parcels leave the screen and return to the TBT with the local screen temperature. Two type-K thermocouples are embedded into the screen radially from opposite sides to monitor the screen temperature. The ends of the thermocouples fall short of the tube centerline by 1.5 mm.

To measure the mean temperature of the gas close to the TBT centerline, special thermocouples were made using 0.13-mm-diameter type-K thermocouple wire welded together to form an approximately 0.4-mm-diameter sphere-like thermocouple junction. The wires are stretched across the TBT and pulled through holes drilled in the tube walls (Fig. 2b). The lowest thermocouple junction is 2.8 mm above the screen, and the remaining 12 thermocouple junctions are equally spaced every 8.1 mm along the TBT. The junctions are intentionally displaced from the tube centerline by 1.5 mm, and the directions of installation are rotated by 90^{o} between subsequent thermocouples so that the wake generated by a thermocouple junction impinges on another junction at least four thermocouples away in either axial direction, a distance typically larger than the acoustic displacement. The wires are fixed in the tube-wall holes by epoxy to seal the high-pressure system and to electrically insulate the thermocouple wires from the tube wall.

Thermal conduction along the thermocouple wires and nonlinear heat transfer between the gas and the thermocouple junction cause the mean temperature of the junction to be slightly different than the mean temperature of the gas at the junction location. To provide an estimate for this difference, a heat balance equation for the junction is averaged over an acoustic period assuming that the junction is in steady state. The heat transfer coefficient for a sphere in steady flow [13] and the quasi-steady approximation are used to calculate the gas-to-junction heat transfer. It is assumed that the gas temperature is not affected by the

presence of thermocouple wires. The time-averaged gas-to-junction heat transfer is balanced against heat conduction between the junction and the TBT walls through the thermocouple wires. The heat transfer between the wires themselves and the gas is ignored because the wires retain an insulating sheath outside the junction region. This estimate shows that the heat leak from the junction to the TBT wall produces a difference between the mean temperatures of the gas and the junction of about 0.1-0.8 K. A correction for this difference is applied to all of the experimental data in this article. The computational procedure to obtain this correction is discussed in Section 4.

The primary sources of error in the measurements of the mean gas temperatures are uncertainties in the gas-to-junction heat transfer coefficient due to variability in the dimensions and shape of the junctions and uncertainties in their positions with respect to the tube centerline. In a separate experiment, three thermocouples were used to measure the radial mean temperature distribution at representative axial locations under acoustic and thermal conditions similar to those used elsewhere in this article. This distribution was then used to estimate the contribution to mean temperature uncertainty due to variations in the radial locations of the thermocouples. The total uncertainty for the temperature measurements is estimated to be approximately 0.4 K for situations with large axial temperature gradients and 0.3 K for near-zero temperature gradients.

In an initial experimental setup, the TBT wall temperature was used as a measure of the mean gas temperature, but the abnormalities observed in the temperature distributions were unexpectedly small, and the temperature profiles were much smoother than anticipated. Estimates showed that the thermal conductance of the walls was high enough (even with only 0.2-mm-thick stainless-steel tube walls) and the heat transfer to the walls low enough that the significant spatial variations in mean gas temperature we expected near the heat exchangers were smeared out. The implementation of the “in-gas” thermocouples is the key to obtaining accurate mean-temperature data for the gas.

This experiment is intended to create quasi-1D conditions for studying the temperature end effect. However, at high acoustic amplitudes, Rayleigh streaming can appear inside the tube, forming a recirculating steady-flow cell. The streaming will not significantly affect the interface process if the penetration of the streaming flow into the end zone during one acoustic cycle is much smaller than the characteristic longitudinal dimension of this zone, which is the peak-to-peak acoustic displacement.

Therefore, the effect of streaming is small if the characteristic streaming velocity is much smaller than the acoustic velocity. The characteristic streaming velocity can be estimated as the effective second-order (with respect to first-order acoustic variables) driving velocity that appears in the vicinity of the outer edge of the boundary layer at the tube wall [14]. When the hot heat exchanger is placed below the cold heat exchanger, buoyancy will further enhance the streaming. This amplification in the presence of gravity has been previously computed [15]. It appears that the most intensive streaming flow in our system is associated with streaming velocities of about 4% of the acoustic velocity amplitude. Analysis based on these considerations shows that we can neglect the effect of acoustic streaming on the interface processes happening inside the end zone. Another estimate can be made for the radial non-uniformity of the screen temperature due to a recirculating streaming flow in the presence of a longitudinal temperature gradient in the tube. Heat conduction in the screen is high enough to limit this radial temperature variation to 0.5 K.

3. Mathematical Model

The mean temperature distribution near the ends of a TBT is determined by the kinematics the gas parcels and their thermal history due to acoustic oscillations and interactions with each other and with the adjacent heat exchanger. In contrast to previous models aimed at explaining temperature overshoots [1,10], we have developed a numerical algorithm for computing the time-averaged temperature in the entire zone from the heat exchanger to a peak-to-peak displacement into the TBT. Beyond this zone the gas parcels do not come into immediate contact with the heat exchanger, and the temperature profile is determined by other factors.

Figure 3 illustrates the framework for our model, which has the same general configuration as already discussed in Fig. 1. We assume that the acoustic flow is one-dimensional and generated by an oscillating solid piston located more than one peak-to-peak displacement to the left of the heat exchanger-TBT interface. All effects of the TBT wall are neglected. The gas is partitioned into a set of N narrow, fixed-mass gas parcels extending from the oscillating piston boundary, $x'_p(t)$, on the left to the vertical plane labeled $x'_N(t)$ on the right that moves with the N-th parcel of gas. Variables x' (with apostrophe) are fixed in the Langrangian frame of reference associated with the gas and vary with time in the Eulerian frame fixed in the laboratory. We chose $x'_N(t)$ to be at least $5x_1$ from the heat exchanger-TBT interface

at its leftmost position, where x_1 is the gas peak displacement evaluated at the heat exchanger-TBT interface, and we chose $x'_p(t)$ so that its time average position is $3x_1$ to the left of the heat exchanger-TBT interface. Both x'_p and x'_N are sufficiently far from the heat exchanger-TBT interface so that numerical results in the region $0 < x < 2x_1$ are not sensitive to the time-averaged positions of x'_p and x'_N. The gas between x'_p and x'_N has a fixed mass, but moves with changing volume as x'_p and x'_N oscillate in the Eulerian frame of reference.

Since the distance between x'_p and x'_N is much smaller than an acoustic wavelength and we are neglecting viscosity, the acoustic pressure amplitude is taken to be uniform between x'_p and x'_N. This assumption holds well in the TBT, but breaks down inside real heat exchangers due to their tight passages. However, we only require the acoustic velocity and the pressure in the TBT, which can be written

$$u(x,t) = u_1(x)\sin(\omega t), \tag{2}$$

$$p(t) = p_m + p_1 \sin(\omega t + \theta), \tag{3}$$

where u_1 and p_1 are real numbers that represent the amplitude of acoustic velocity and pressure, respectively, ω is the angular frequency, and θ is the phase by which the pressure oscillations lead the velocity oscillations. Our model includes spatial variations in u_1 due to the compressibility of the gas, so the motion of the piston is selected to produce the experimental u_1 and θ at the interface.

The *i*-th parcel of the gas (counting starts from the slice adjacent to the piston) is characterized by several parameters: mass per unit cross-sectional area m_0 (the same for all parcels, and independent of time), temperature $T_i(t)$ (assumed spatially uniform within the parcel), parcel width $h_i(t)$, and the coordinate of the right boundary of the parcel $x'_i(t)$. The evolution of the parcel width depends on its density

$$\frac{dh_i}{dt} = -\frac{m_0}{\rho_i^2}\frac{d\rho_i}{dt}. \tag{4}$$

Assuming that the gas is ideal, the equation of state written for the *i*-th parcel is

$$p = \rho_i R T_i, \tag{5}$$

where R is the specific gas constant. Using Eq. (5) and mass conservation, the dynamics of the parcel width is given by

$$\frac{dh_i}{dt} = \frac{m_0 R}{p}\left(\frac{dT_i}{dt} - \frac{T_i}{p}\frac{dp}{dt}\right), \tag{6}$$

where the full pressure $p(t)$ is given by Eq. (3). The position of the parcel's right boundary is given by

$$x'_i = x'_p + \sum_{j=1}^{i} h_j \,, \tag{7}$$

where $x'_p(t)$ is the position of the piston obtained by using Eq. (2) and the time-averaged piston position $\overline{x'_p} = -3x_1$. If the temperature of each gas parcel was known, Eqs. (6) and (7) fully describe kinematics of the parcels. Additionally, Eqs. (6) and (7) satisfy mass conservation exactly.

Including acoustic pressure oscillations, heat conduction between adjacent gas slices, and thermal contact with the heat exchanger in the First Law of thermodynamics, the time derivative of the temperature of a gas parcel is

$$\frac{dT_i}{dt} = \frac{\gamma - 1}{\gamma}\frac{T_i}{p}\frac{dp}{dt} + \frac{k}{c_p}\frac{RT_i}{p}\left(\frac{\partial^2 T}{\partial x^2}\right)_i + K_i\left(T_{HX} - T_i\right), \tag{8}$$

where k and c_p are the thermal conductivity and specific heat at constant pressure, respectively. The heat capacity is evaluated at T_{HX}, while an estimate of the thermal conductivity is given in the next section. The second spatial derivative of the temperature is approximated by

$$\left(\frac{\partial^2 T}{\partial x^2}\right)_i \approx \frac{2}{h_i}\left(\frac{T_{i+1} - T_i}{h_{i+1} + h_i} - \frac{T_i - T_{i-1}}{h_i + h_{i-1}}\right). \tag{9}$$

The last term in Eq. (8) describes the heat transfer between the parcel and the heat exchanger. If the parcel is completely inside the heat exchanger, the coefficient K_i in Eq. (8) is equal to the effective heat transfer coefficient between the parcel and the heat exchanger, K_0. If the parcel is only partially inside, K_i is simply a weighted average of K_0 for the fraction of the parcel inside of the heat exchanger and 0 for the fraction outside, i.e.,

$$K_i = \begin{cases} K_0, & x'_i < 0 \\ K_0 \dfrac{h_i - x_i}{h_i}, & x'_i > 0,\ x'_{i-1} < 0 \\ 0, & x'_{i-1} > 0 \end{cases} . \tag{10}$$

High values of K_0 make the volume inside of the heat exchanger more isothermal.

An initial instantaneous temperature distribution is assigned to the gas parcels, and Eqs. (6) and (8) are integrated in time. The instantaneous mean temperature in Eulerian coordinates is computed by linearly interpolating between adjacent Lagrangian parcels and averaging over an acoustic cycle. The numerical integration proceeds until this cycle-averaged Eulerian mean temperature reaches a steady state. The initial temperature of the *N*-th parcel on the right boundary of the computational domain is selected to generate a mean temperature gradient just outside of $2x_1$ that matches the experimental data. This parcel, which is far enough beyond $2x_1$ that its temperature oscillations do not directly affect the mean temperature for $x < 2x_1$, is assumed to oscillate adiabatically. The thermal boundary condition on the left side is the temperature of the heat exchanger T_{HX}. The heat transfer parameter K_0 is chosen to be $1/\Delta t$ (see below), which is the highest value that does not cause a numerical instability. It is large enough to ensure that the parcels that never leave the heat exchanger always have a temperature very close to T_{HX}.

Time stepping in the numerical simulation is carried out utilizing the predictor-corrector method [16]. The time step, Δt, and the mass per unit area of a gas parcel in the heat exchanger, m_0, were varied until the numerical code generated a converged solution. The convergence of the code was checked by ensuring that the steady-state numerical results gave zero time-averaged mass flux everywhere in the computational domain and a constant time-averaged enthalpy flux outside the heat exchanger. The time-averaged mass and enthalpy flux are given by

$$\dot{m}(x) = \frac{1}{\tau}\int_0^{\tau} \rho(x,t)\,u(x,t)\,dt \tag{11}$$

$$\dot{H}(x) = \frac{1}{\tau}\int_0^{\tau} \left[\rho(x,t)\,u(x,t)T(x,t)\,c_p + k\frac{\partial T(x,t)}{\partial x} \right] dt , \tag{12}$$

where $\tau = 2\pi/\omega$ is the cycle period, and all variables are determined in Eulerian coordinates. In addition, the integration time was increased until the time-averaged temperature gradient beyond the peak-to-peak

displacement in Eulerian coordinates changed by less than 10^{-2} K/m from one cycle to the next. Further increases in the integration time did not result in a significantly different steady-state solution. Our convergence study yielded a time step of $\Delta t = \tau / 200$ and a mass per unit area of a gas parcel of $m_0 = \rho x_1 / 10$ (evaluated at the heat exchanger temperature). The finite spatial discretization causes an error in the mean temperature profile within about one parcel width of the heat exchanger-TBT interface, but outside of this short interval the mean temperature profile is not sensitive to reductions in m_0 below the chosen value.

4. Methodology

Equation (1), which predicts the mean-temperature discontinuity at the heat exchanger-TBT interface, shows that some of the independent variables of interest are p_1 / p_m, x_1, θ, and dT_m / dx. We expect these variables will also control the temperature distribution between $x = 0$ and $2x_1$. Therefore, we varied each of these four variables while holding the other three constant. We also varied γ by using nitrogen instead of helium, but those results are not presented here. The other parameter in Eq. (1), T_{HX}, was varied to help establish a certain dT_m / dx: the highest T_{HX} corresponded to the minimum dT_m / dx, and vice versa. To achieve different acoustic conditions in the experiment, we varied the electrical drive level to the linear motor, the drive frequency (between 38 and 68 Hz), and the setting of the two network valves. Also, the experimental section could be placed above the lower heat exchanger or below the upper heat exchanger, which allowed θ to be changed by approximately 180^o.

Using the measured complex pressure amplitudes in the tank and at the lower heat exchanger, a numerical model [12] is used to infer p_1, u_1, and θ throughout the experimental section. The inertance and resistance of the components between the pressure sensor at the acoustic network entrance and the experimental section are low enough that the changes in the acoustic pressure amplitude and phase over this distance are less than 8% and $4°$, respectively. Additionally, the volume of the gas in the inertance line and lower heat exchanger is small enough that the changes in the acoustic velocity amplitude and phase between the tank and the test section are less than 20% and $10°$, respectively. We believe uncertainties in our determinations of p_1, u_1, and θ to be less than 1.2%, 1.3%, and $2.2°$, respectively. The heat

exchangers at either end of the TBT are used to regulate the temperature gradient in the TBT. The maximum temperature is restricted by the epoxy that holds the thermocouple wires in the walls of the TBT, and the minimum temperature is limited by the cooling water used to extract heat from the heat exchangers.

The screen at the end of the experimental region (Fig. 2b) approximates an ideal heat exchanger. However, in high-power regimes, axial energy flux through the system generates a significant axial temperature gradient in the screen. Using the temperatures measured by the two thermocouples embedded in the screen, we can extrapolate to obtain the screen temperature at the interface, but the axial temperature gradient in the screen results in high uncertainty of the interface temperature (see figures in next section). Instead of this temperature, the gas temperature at $2x_1$ into the TBT is used to match the measurements to the numerical simulations. We hope that future experimenters will devise a way to enforce a smaller axial temperature gradient in the heat exchanger or to measure the interface temperature more accurately.

The other thermal boundary condition is the time-averaged temperature gradient just beyond $2x_1$. From known velocity and adiabatic temperature oscillations outside $2x_1$, the differences between the mean temperatures of the gas and thermocouples in this region are computed as discussed in Section 2. Then, the mean temperature and the temperature gradient of the gas at $2x_1$ are determined by a least-squares linear fit to the corrected temperatures of thermocouples between $2x_1$ and $4x_1$.

These experimental thermal boundary conditions are inputs to the numerical model described in Section 3. The calculated temperature of the heat exchanger and the calculated temperature distribution from 0 to $2x_1$ are the predictions of the calculation that are compared with measurement. There are uncertainties in the computed mean temperature distributions caused by errors in the experimentally determined thermal boundary conditions and in the acoustic parameters. The calculated profiles presented in the next Section have uncertainties that are approximately two times larger than those of the measured temperatures themselves.

Almost all previous analyses of the temperature end effect ignored the heat conduction inside the gas, assuming that the acoustic pressure fluctuations and the interactions between the gas and the heat exchanger dominate. Molecular heat conduction in the gas is likely to have a small effect, but small-scale turbulent eddies created by the screen will cause a significant increase in the effective thermal conductivity.

Landau and Lifshitz [17] estimate the effective thermal conductivity, k_{ef}, in a gas with non-uniformities in velocity Δu over a characteristic dimension l to be

$$k_{ef} \sim \rho c_p \Delta u \, l \, . \tag{13}$$

We take $\Delta u \sim 6$ m/s, which is the characteristic amplitude of the acoustic velocity, and $l \sim 1.2$ mm, as the wire-to-wire spacing in the mesh, which is the relevant length scale of eddies produced by the screen. The resulting effective thermal conductivity becomes $k_{ef} \sim 100\, k_0$ where k_0 is the molecular thermal conductivity. No attempt was made in this study to provide more sophisticated algorithms for computing k_{ef} that could, in principle, include effects such as the time variation of u and vortex dissipation. In the analysis of the data, two sets of simulations are carried out; one with $k = 0$ and a second with $k = 100 k_0$. Both are plotted in Figs. 4 through 7 in the next Section.

In computing the mean temperature profile from 0 to $2x_1$, the time-varying temperatures at the locations of thermocouples in this zone are also calculated. These temperature oscillations, which are non-sinusoidal due to the proximity of the heat exchanger, are used to calculate the difference between the mean temperature of the gas and the thermocouple junctions inside $2x_1$ interval as discussed in Section 2. The molecular thermal conductivity is used to compute the heat transfer between the gas and the junctions. Although Figs. 4 through 7 present calculations for $k = 0$ and $100 k_0$, we only present corrected data for $k = 100 k_0$. Data corrected using $k = 0$ only differs from the $k = 100 k_0$ data by 0.1-0.2 K.

All of the data presented in this article were taken using helium as the working gas. We also carried out several tests with nitrogen and argon, and the agreement between experimental data and model results for these gases was similar to that of helium.

5. Results

In each set of data, only one of the three acoustic parameters is varied, i.e., p_1, x_1, or θ, while the other two are held fixed. For each acoustic condition, we report data for the most negative and most positive temperature gradients that could be produced, as well as a gradient near zero. The solid circles in Fig. 4 are the measured time-averaged gas temperature for p_1 equal to 3% and 6% of $p_m = 345$ kPa and

$\theta = 0°$. To achieve these conditions, the experimental section of the TBT is positioned below the upper experimental heat exchanger. The open squares are the temperatures inside the screen measured by two thermocouples embedded in the screen. The long-dashed and solid lines are simulation results for $k = 0$ and $k = 100\,k_0$, respectively. The short-dashed line is an extrapolation of the temperature distribution beyond $2x_1$ back to $x = 0$. As illustrated schematically in Fig. 1c, the test data in Fig. 4 clearly demonstrate a dip in the mean temperature between $x = 0$ and $2x_1$ driven by the decrease in the acoustic pressure after the parcels exit the heat exchanger. Comparing data at p_1 / p_m of 3% and 6% for low temperature gradients where the $x_1 \frac{dT_m}{dx}$ term in Eq. (1) is small clearly shows the effect of the magnitude of p_1: the dip in mean temperature in Fig. 1e is twice that of Fig. 1b. The deviation of the mean temperature from a linear distribution ends at $2x_1$. The discrepancies in Figs 4c and 4f may be due to the mean temperature distribution being unstable with respect to gravity-driven convection.

The numerically generated temperature distributions for $k = 0$ show qualitative agreement with the data, but the results for $k = 100\,k_0$ are clearly in better quantitative agreement. The enhanced thermal conductivity smoothes out the rapid spatial variations in the mean temperature calculated with $k = 0$. The simulation results for the heat exchanger temperature are in reasonable agreement with the measured screen temperatures (that could be extrapolated from two in-screen measured points), given the large uncertainty in the screen temperatures as described above. These temperatures (open squares) are plotted on this and the following figures for illustration only.

Figure 5 shows the mean temperature profiles obtained at $p_1 / p_m = 5\%$, and $\theta = 0°$, but Figs. 5a and b have $2x_1 = 7.18$ cm while Figs. 5c and d have $2x_1 = 3.13$ cm. The general behavior of the temperature distribution is similar to that in Fig. 4, and Figs. 5a and b again clearly demonstrate that the region affected by interaction with the heat exchanger ends at $2x_1$. The small number of points beyond the peak-to-peak displacement may cause inaccuracy in determining the external temperature gradient in Figs. 5a and b. The data points are too sparse in Figs. 5c and d to make a definite conclusion for small displacement amplitudes. Numerical simulations with $k = 100\,k_0$ produce slightly better agreement with experimental

data than those with zero heat conduction. (We have used the same value of k in each simulation even though u_1 differs by a factor of 1.5 between the large and small $2x_1$ cases.)

With reasonable correlation between the measured and simulated mean temperature distributions for variations in p_1 / p_m and $2x_1$, we study the effect of variations in θ. The results for $\theta = -25°$ and $45°$ and $p_1 / p_m = 5\%$ are given in Fig. 6. Although the measured temperature distributions show some similarity with the $\theta = 0°$ data in Fig. 4, there is noticeable evolution as the phase deviates in either direction from zero. The agreement between the results of simulations with enhanced heat conduction and experimental data is good for most temperature gradients in Fig. 6.

By positioning the experimental section of the TBT near the lower heat exchanger, it is possible to change θ by nearly $180°$. Results shown in Fig. 7 are taken with $p_1 / p_m = 5\%$ and $\theta = -180°$, $p_1 / p_m = 6\%$ and $\theta = -150°$, and $p_1 / p_m = 5\%$ and $\theta = -120°$. With θ changed by $\sim 180°$, the acoustic pressure increases after the parcel leaves the heat exchanger, resulting in an increase in mean temperature between $x = 0$ and $2x_1$. The experimental data continue to evolve gradually as the phase is varied away from $-180°$, but the agreement with the simulations becomes poorer. The discrepancy is generally small for $\theta = -180°$, but it starts to grow at phase $-150°$ and becomes large at $\theta = -120°$. Reasons for this disagreement are unknown. It is possible that, when approaching the boundary of the achievable acoustic domain (in our apparatus), the experimental errors are larger. Further investigations with standing wave phasing are needed to clarify this disagreement.

6. Conclusions

The mean gas temperature distribution within one peak-to-peak gas displacement of the ends of a thermal buffer tube or pulse tube is determined by the interaction of the gas with the adjacent heat exchanger, the adiabatic motion of the gas once it exits the heat exchanger, and turbulence-enhanced thermal conduction between gas parcels along the axis of oscillation. The mean temperature distribution beyond one peak-to-peak gas displacement only affects the mean temperature inside $2x_1$ by setting thermal boundary conditions on the gas inside $2x_1$.

Measurements of the mean gas temperature within one peak-to-peak displacement from the interface between a TBT (or pulse tube) and a heat exchanger are made for various values of the acoustic pressure, acoustic displacement (velocity), the phase between pressure and velocity, and the mean temperature gradient outside of one peak-to-peak displacement. Our numerical model includes the kinematics of the gas parcels, thermal interaction with the adjacent heat exchanger, and heat conduction between gas parcels. The gas's thermal conductivity is enhanced due to turbulent eddies generated by the acoustic flow through the screens that comprise the heat exchanger. This leads to a significant smoothing of the rapid spatial variations in mean temperature that would be expected if the gas's thermal conductivity were simply given by the molecular value.

The model results for the mean gas temperature are in good quantitative agreement with the data when the phase between the acoustic pressure and the velocity is $0°$ or $180°$. As the phase is varied away from these values, the agreement becomes progressively worse. The cause of this deviation is a mystery to us.

By making a heat exchanger composed of thin surfaces parallel to the acoustic motion, it may be possible to minimize the eddy production in the acoustic flow, and, therefore, to reduce uncertainties related to the heat transfer enhancement by eddies. On the other hand, by introducing more sophisticated algorithms for computing the effective local thermal conductivity, one may achieve a better agreement between test data and model results. The acoustic network can be modified to approach a standing wave phasing, where unresolved mysteries are found. Accurately measuring the temperature distribution in the screen, especially close to the interface with the tube, remains a significant experimental challenge. Such measurements would improve the model validation and may motivate model modification.

Acknowledgements

This work was supported by the Office of Basic Energy Sciences, Division of Materials Science, in the US Department of Energy's Office of Science.

References

[1] G.W. Swift, Thermoacoustics: A Unifying Perspective for Some Engines and Refrigerators, Acoustical Society of America, Sewickley, PA, 2002.

[2] In pulse tube refrigerators, these tubes are called "pulse tubes" for historical reasons, even for sinusoidal pressure and motion in which no pulses exist. For simplicity in this paper, the more general term "thermal buffer tubes" should be understood to include such pulse tubes.

[3] J.L. Smith, M.J. Romm, Thermodynamic loss at component interfaces in Stirling cycles, in: Proceedings of the Twenty Seventh Intersociety Energy Conversion Engineering Conference, Society of Automotive Engineers, 1992, pp. 5.529-5.532.

[4] M.J. Romm, J.L. Smith, Stirling engine losses in dead volumes between components, in: Proceedings of the Twenty Eighth Intersociety Energy Conversion Engineering Conference, American Chemical Society, 1993, pp. 2.751-2.758.

[5] L. Bauwens, Stirling cryocooler model with stratified cylinders and quasisteady heat exchanger, Journal of Thermophysics and Heat Transfer 9(1) (1998) 129-135.

[6] L. Bauwens, Interface loss in the small amplitude orifice pulse tube model, in: P. Kittel (Ed.), Advances in Cryogenic Engineering, Vol. 43, Plenum Press, New York, 1998, pp. 1933-1940.

[7] P.J. Storch, R. Radebaugh, J.E. Zimmerman, Analytical model for the refrigeration power of the orifice pulse tube refrigerator, Technical note 1343, National Institute of Standards and Technology, 1990.

[8] G.W. Swift, Analysis and performance of a large thermoacoustic engine, Journal of the Acoustical Society of America 92 (1992) 1551-1563.

[9] P.C.T. de Boer, Thermodynamic analysis of the basic pulse-tube refrigerator, Cryogenics 34 (1994) 699-711.

[10] P. Kittel, The temperature profile within pulse tubes, in: P. Kittel (Ed.), Advances in Cryogenic Engineering, Vol. 43, Plenum Press, New York, 1998, pp. 1927-1932.

[11] D.L. Gardner, G.W. Swift, Use of inertance in orifice pulse tube refrigerators, Cryogenics 37 (1997) 117-121.

[12] W.C. Ward, G.W. Swift, Design environment for low-amplitude thermoacoustic engines, Journal of the Acoustical Society of America 95 (1994) 3671-3672. Software and user's guide available from

www.lanl.gov/thermoacoustics/ or from the Energy Science and Technology Software Center, Oak Ridge, TN.

[13] A.F. Mills, Heat and Mass Transfer, Irwin, Chicago, 1995, equation (4.76).

[14] J.R. Olson, G.W. Swift, Acoustic streaming in pulse tube refrigerators: tapered pulse tubes, Cryogenics 37 (1997) 769-776.

[15] K.I. Matveev, S. Backhaus, G.W. Swift, The effect of gravity on heat transfer by Rayleigh streaming in pulse tubes and thermal buffer tubes, in: Proceedings of International Mechanical Engineering Congress and Exposition, American Society of Mechanical Engineers, 2004, IMECE 2004-59076.

[16] J.H. Ferziger, M. Peric, Computational Methods for Fluid Dynamics, Springer-Verlag, New York, 1999.

[17] L.D. Landau, E.M. Lifshitz, Fluid Mechanics, Pergamon Press, Oxford, 1987, § 54.

Figure captions:

Fig. 1 (adapted from [1]). (a) Schematic drawing of the interface between a TBT and a heat exchanger. The peak-to-peak displacement of a gas parcel is $2x_1$. (b) Temperature–position trajectories for gas parcels undergoing acoustic motion with pressure lagging velocity by $90°$. T_{HX} is the heat exchanger temperature and $T_m(x)$ is the mean temperature of the gas. The lines show the temperature–position trajectories for various gas parcels. The trajectory of the "particular" parcel that just enters the heat exchanger at its leftmost position is shown in bold. A bold line also marks T_{HX} inside the heat exchanger. δT_m is the temperature discontinuity between the heat exchanger and the mean gas temperature, extrapolated from beyond $2x_1$, as calculated in [1]. (c) Same as (b) except for acoustic motion with pressure and velocity in phase.

Fig. 2. Schematic of the apparatus (not to scale). (a) Overall thermoacoustic system. "P" indicates locations of pressure sensors. (b) Magnified view of experimental zone. The solid and dashed lines represent wires that that are above and below the plane of the Figure, respectively. The wires leading to thermocouple junctions depicted without such lines are oriented perpendicular to the plane of the figure. O-rings and bolts are not shown.

Fig. 3. Numerical model computational space. The instantaneous positions of the piston and the right edge of the rightmost gas parcel are x'_p and x'_N, respectively. The interface between the heat exchanger and the TBT is at $x = 0$.

Fig. 4. Mean temperature profiles in the gas near the screen interface with $2x_1 = 4.75$ cm and $\theta = 0°$. (a), (b), (c) $p_1 / p_m = 0.03$; (d), (e), (f) $p_1 / p_m = 0.06$. Dash-dotted vertical lines indicate the heat exchanger interface (at $x = 0$) and the peak-to-peak displacement from the heat exchanger interface into the TBT (near $x = 4.75$ cm). •, measurements of gas mean temperature using the thermocouple junctions suspended in

the TBT; □, temperature measured by thermocouples embedded in the screen; dotted line, the linear temperature profile estimated by extrapolating the mean temperature beyond the peak-to-peak displacement back to the heat exchanger interface; dashed line, calculated mean temperature profile using $k = 0$; solid line, calculated mean temperature profile using $k = 100k_0$. The measurement uncertainties are 0.4 K (for cases with significant temperature gradient) and 0.3 K (for near-zero temperature gradient); uncertainties in the calculated profiles are approximately two times larger.

Fig. 5. Mean temperature profiles in the gas near the screen interface at $p_1 / p_m = 0.05$ and $\theta = 0°$. (a), (b) $2x_1 = 7.18$ cm; (c), (d) $2x_1 = 3.13$ cm. All symbols are the same as in Fig. 4.

Fig. 6. Mean temperature profiles in the gas near the screen interface at $p_1 / p_m = 0.05$ and $2x_1 = 4.75$ cm. (a), (b), (c) $\theta = -25°$; (d), (e), (f) $\theta = 45°$. All symbols are the same as in Fig. 4.

Fig. 7. Mean temperature profiles in the gas near the screen interface at $2x_1 = 4.75$ cm. (a), (b), (c) $p_1 / p_m = 0.05$ and $\theta = -180°$; (d), (e), (f) $p_1 / p_m = 0.06$ and $\theta = -150°$; (g), (h), (i) $p_1 / p_m = 0.05$ and $\theta = -120°$. All symbols are the same as in Fig. 4.

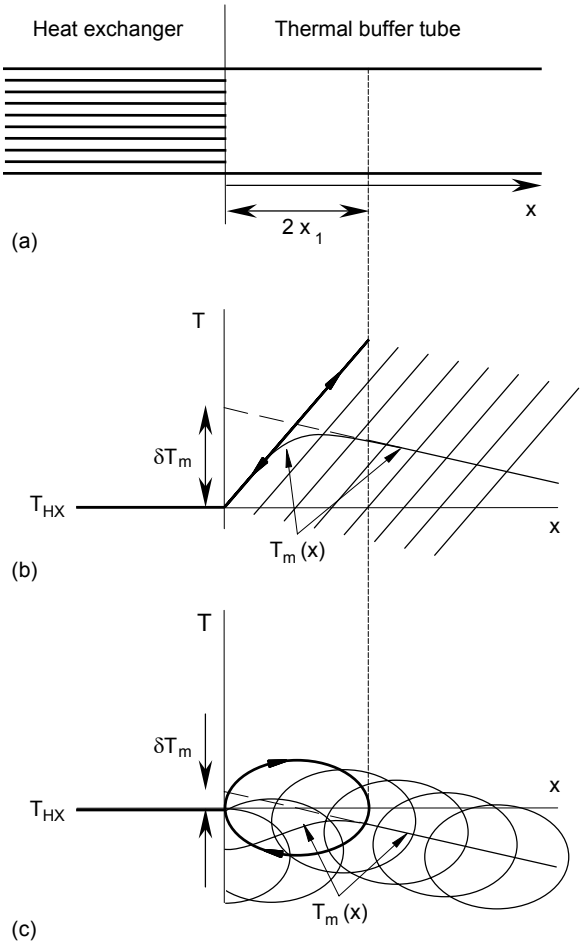

Figure 1. Matveev, Swift, and Backhaus.

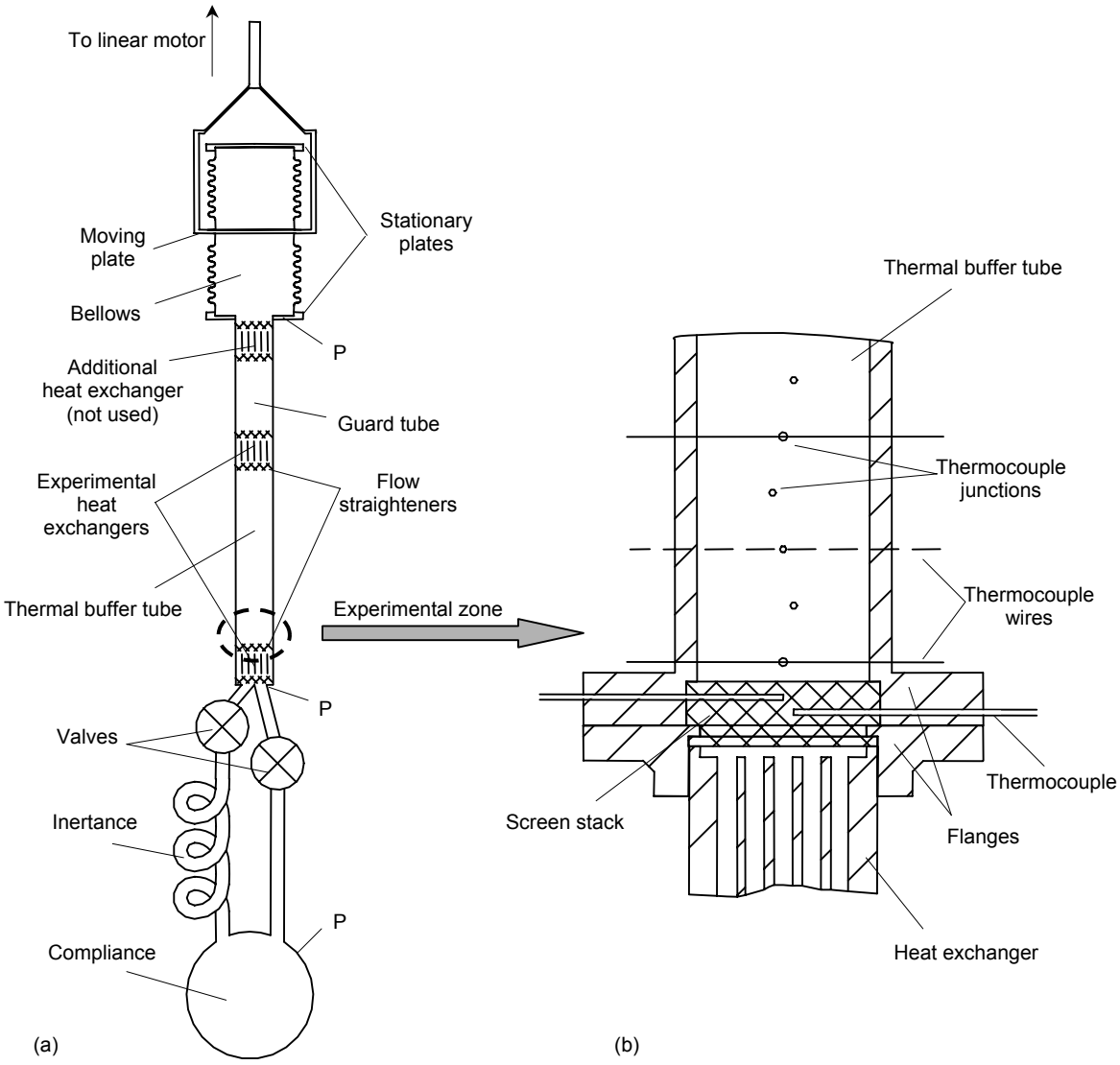

Figure 2. Matveev, Swift, and Backhaus.

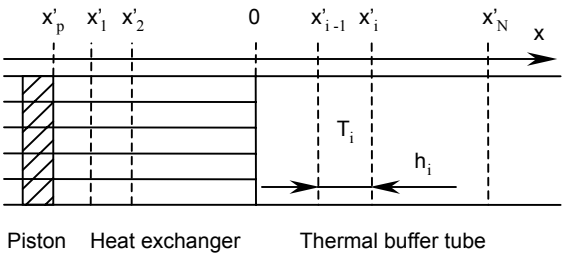

Figure 3. Matveev, Swift, and Backhaus.

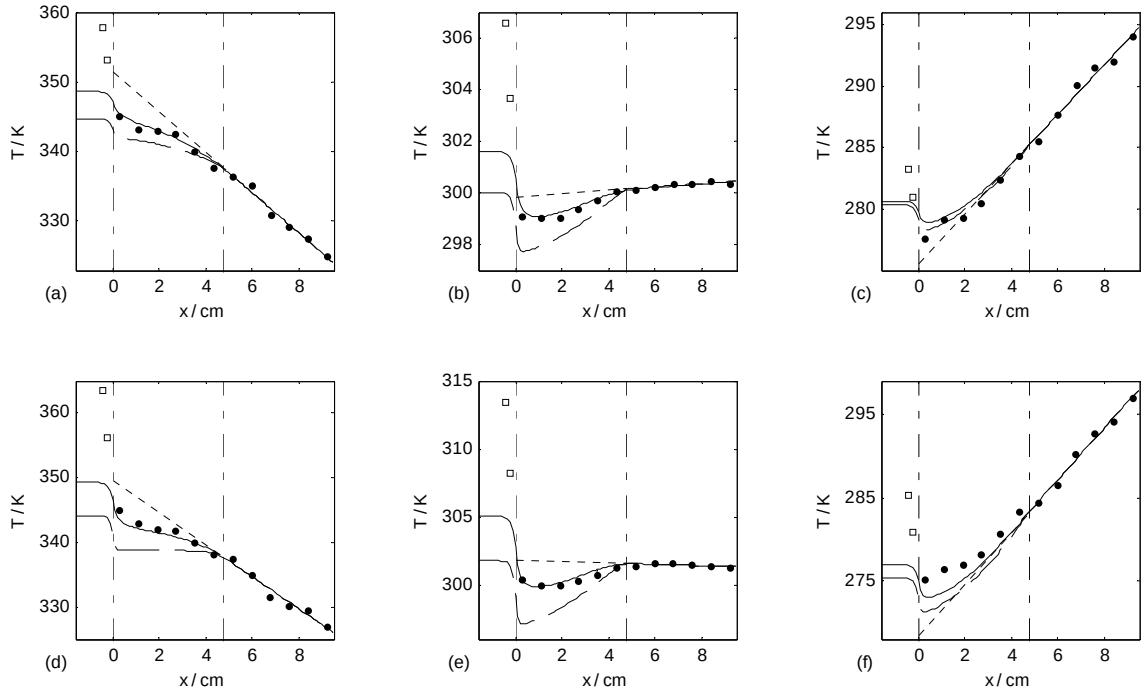

Figure 4. Matveev, Swift, and Backhaus.

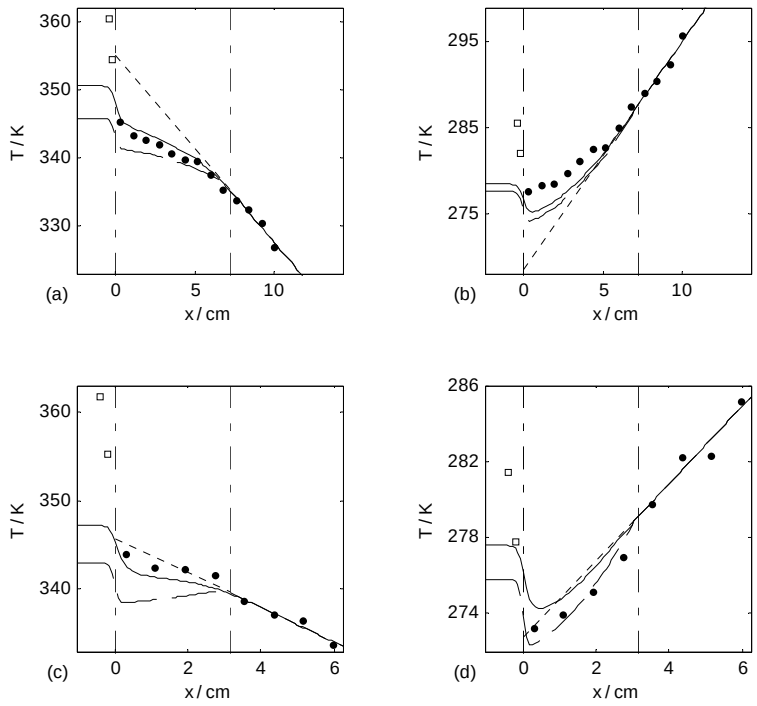

Figure 5. Matveev, Swift, and Backhaus.

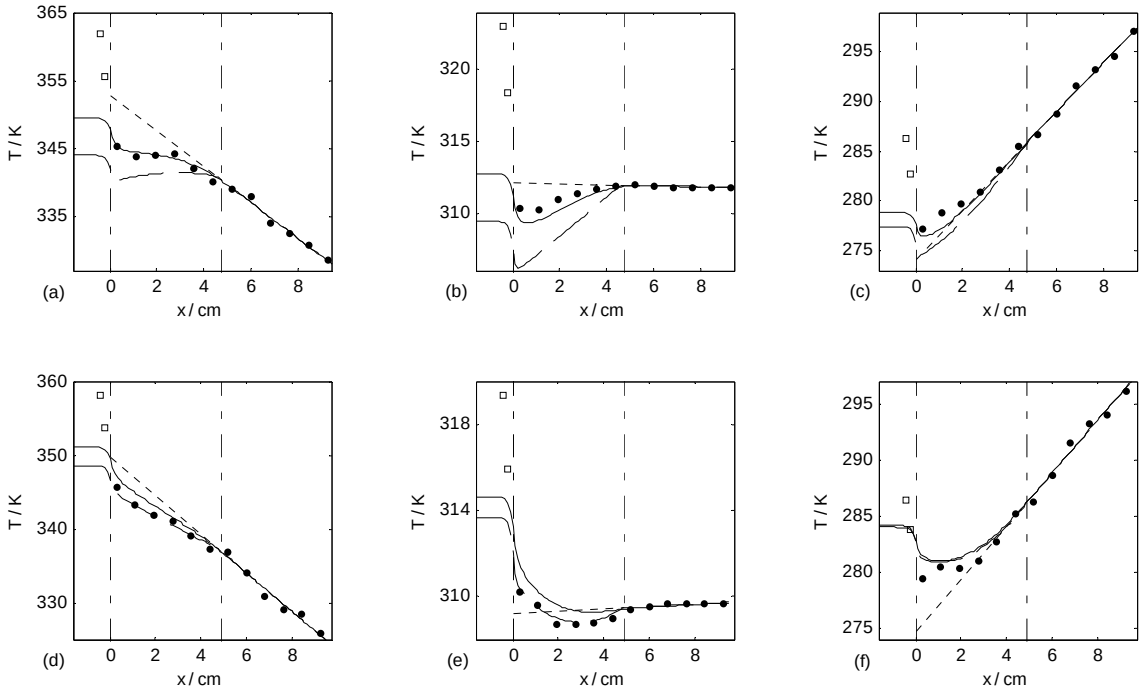

Figure 6. Matveev, Swift, and Backhaus.

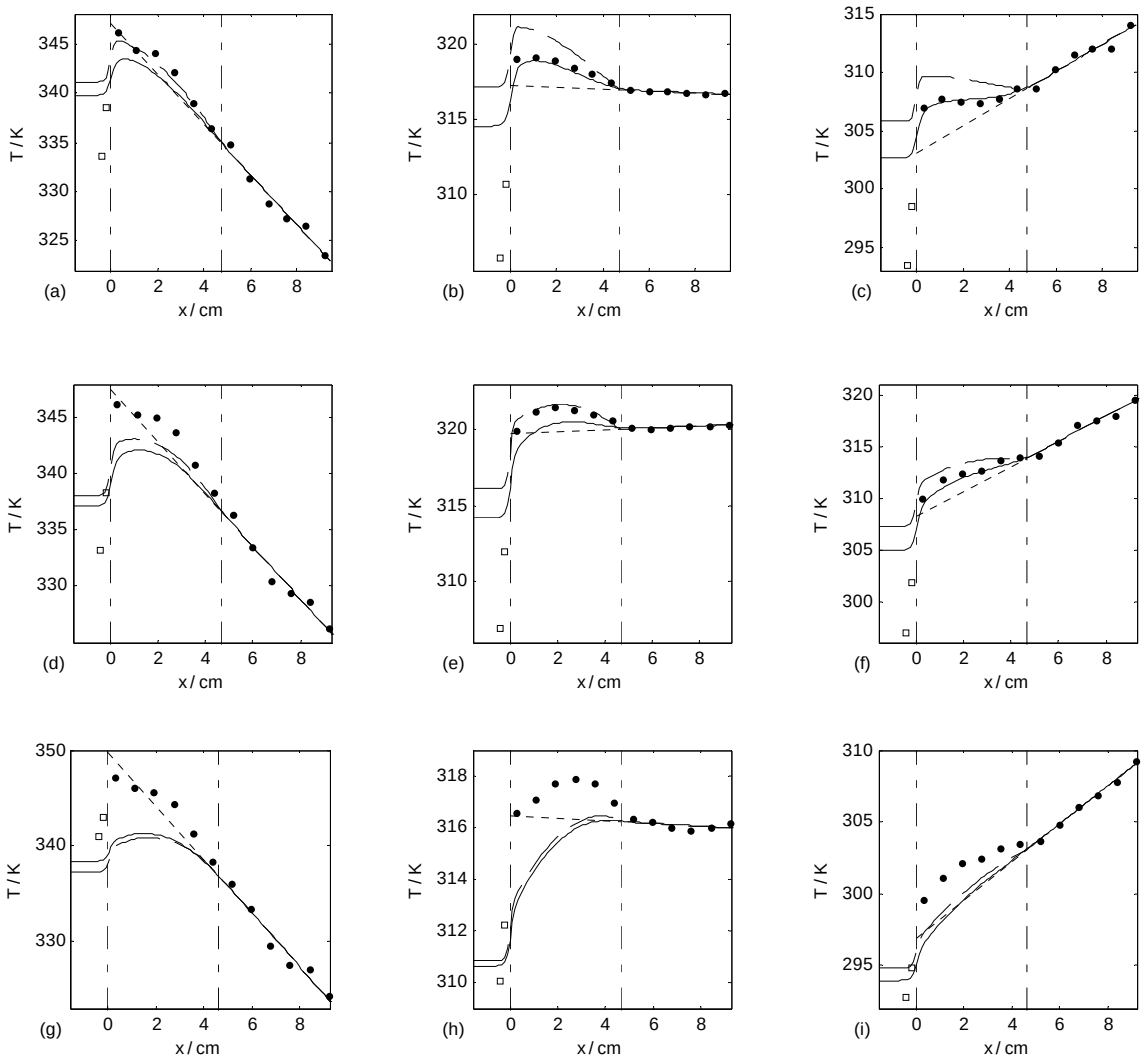

Figure 7. Matveev, Swift, and Backhaus.